applied sciences

MDPI

Article

Hydrodynamic Ram Effect Caused by Debris Hypervelocity Impact on Satellite Tank

Beilei Zhao [1,*], Jiguang Zhao [2], Cunyan Cui [1] and Yongsheng Duan [1]

1 Department of Aerospace Science and Technology, Space Engineering University, Beijing 101416, China; ccy6655@126.com (C.C.); duanys_vip@yeah.net (Y.D.)
2 Department of Electronic and Optical Engineering, Space Engineering University, Beijing 101416, China; zhaoyy8600@139.com
* Correspondence: khy-lmj@alumni.sjtu.edu.cn; Tel.: +86-188-1096-2461

Received: 5 September 2019; Accepted: 7 October 2019; Published: 9 October 2019

check for updates

Featured Application: Numerical simulation of the debris impacting the satellite tank at the velocity of 7000 m/s was carried out based on ANSYS/LS-DYNA software. The structural damage to the satellite tank caused by the hydrodynamic ram effect was analyzed, the influence of the angular velocity of debris on the hydrodynamic ram effect was studied. The conclusions are of great significance for the risk assessment of the satellite.

Abstract: To study the hydrodynamic ram effect caused by the debris hypervelocity impact on the satellite tank, a numerical simulation of the spherical debris impacting the satellite tank at the velocity of 7000 m/s was carried out based on ANSYS/LS-DYNA software. The attenuation law of debris velocity, the propagation process of the shock wave and the deformation of the tank walls were investigated. The influences of the liquid-filling ratio, the magnitude, and direction of angular velocity on the hydrodynamic ram effect were analyzed. Results show that the debris velocity decreased rapidly and the residual velocity was 263 m/s when the debris passed through the tank. The shock wave was hemispherical, and the pressure of shock wave was the smallest at the element with an angle of 90° to the impact line. The maximum diameter of the front perforation was larger than that of the back perforation and the bulge height on the front wall was smaller than that on the back wall. With the decrease of the liquid-filling ratio, the diameter of the perforations and bulge height decreased. When the debris impacted the satellite tank with the angular velocity in the x direction, the debris trajectory did not deflect. When the debris impacted the satellite tank with the angular velocities in the y and z direction, the debris trajectory deflected to the negative direction of the z axis and y axis, respectively. The magnitude of the angular velocity affects the residual velocity of debris and the diameter of perforations.

Keywords: debris; hypervelocity impact; satellite tank; hydrodynamic ram effect; numerical simulation

1. Introduction

Collisions between satellites and space debris are likely to occur given the rapid increase in space debris [1]. The satellite tank is filled with liquid hydrazine, which accounts for a large part of the total mass, and is one of the most vulnerable components to debris impact. When the debris impacts the satellite tank, a shock wave is generated in the liquid hydrazine. Debris penetration and shock wave pressure act on the tank walls, causing catastrophic damage to the tank structure. This phenomenon is known as the hydrodynamic ram effect.

Since the 1970s, the hydrodynamic ram effect has been the subject of many investigations. Scholars have focused on the hydrodynamic ram effect caused by the fragment impact on aircraft fuel tanks [2,3] or ship defensive cabins [4]. The deformation of tank walls, the shock wave pressure, and the velocity attenuation of the fragment have been studied. As the hydrodynamic ram effect involves the shock stage, drag stage, cavity stage, and exit stage [5], it can be complicated to describe each stage in theory. Tests and numerical simulation are the main research methods.

Disimile P.J. [6] performed a series of tests where a tungsten projectile, steel projectile, and aluminum projectile were shot into a liquid-filled tank at the velocities of 341 m/s, 389 m/s, and 455 m/s. The shock wave pressures at different positions were measured. Townsend D. et al. [7] carried out tests in which projectiles weighting 3.5 g and 7 g were accelerated to velocities between 1000 m/s and 3000 m/s to impact water-filled tanks and the movement of the projectiles and the plastic deformation of the tank walls were recorded. Nishida M. et al. [8] conducted tests in which spherical projectiles were launched at velocities from 40 m/s to 200 m/s against an aluminum square tube filled with water to explore the relationship between the square tube perforation, material strength, and projectile diameter. Varas D. et al. [9] used the steel projectiles with the diameter of 12.5 mm moving at velocities of 600 m/s and 900 m/s to impact an aluminum vessel filled with water. The effects of the liquid filling ratio and impact velocity on wall deformation were investigated. Ma L.Y. et al. [10] performed a test where a steel projectile with the diameter of 9.5 mm was shot into an aluminum vessel filled with water at the velocity of 686 m/s and the length and diameter of the cavity were recorded by a high-speed camera.

With the advantages of low cost, good repeatability, and easy access to intermediate quantities, numerical simulation has been widely used. Based on the smoothed particle hydrodynamics (SPH) algorithm in AUTODYN software, Kong X.S. et al. [11] conducted numerical simulation where two fragments impacted the liquid-filled cabin at the velocity of 2000 m/s simultaneously. The influence of the interval between two fragments on the superposition of shock waves was investigated. Aziz M.R. et al. [12] carried out a numerical simulation where the projectile impacted the water-filled tank at the velocity of 972 m/s using the coupling algorithm of finite element method (FEM) and SPH. The pressure–time curve obtained by the simulation agreed well with the test results. Kangjie R.Y. et al. [13] simulated projectiles impacting the water-filled tank at the velocity of 250 m/s and 300 m/s based on the MSC/Dytran program, and analyzed the dynamic response of the entry wall and the exit wall. Varas D. et al. [5,14] used the arbitrary Lagrangian–Eulerian (ALE) algorithm and SPH algorithm to reproduce the projectiles impacting the 60%, 75%, and 100% water-filled tank at the velocity of 600 m/s and 900 m/s. Results showed that the shock wave pressure calculated by the ALE algorithm was more accurate than the SPH algorithm. Han L. et al. [15] simulated the impact of fragments on an aircraft fuel tank based on ANSYS/LS-DYNA software. The influence of the velocity, mass, shape, and incident angle of the fragment on the hydrodynamic ram effect were analyzed.

In the above studies, the impact velocities were less than 3000 m/s, but the velocity of space debris can reach more than 7000 m/s, which belongs to hypervelocity. At the end of the 20th century, the National Aeronautics and Space Administration (NASA) carried out a series of hypervelocity impact tests to study the damage consequences of hypervelocity impact on spacecraft. In 1991, the White Sands Test Facility (WSTF) participated in a joint test program with the NASA Hypervelocity Impact Research Laboratory (HIRL) [16] where they used an aluminum projectile with the diameter of 0.318 cm moving at velocities from 6000 m/s to 6400 m/s to impact a vessel filled with liquid hydrazine. Circular perforations, petal-shaped bulges, and cracks were observed on the entry and exit walls. In the same year, the Science Applications International Corporation (SAIC) also performed a test in which a cylindrical projectile weighting 100 g was launched at a velocity of 5000 m/s against a 100-mm-diameter vessel filled with liquid hydrazine [17]. The results indicated that some reaction occurred in the liquid hydrazine, but not enough evidence was gathered to confirm a detonation.

Hypervelocity impact is characterized by a short duration, high pressure, and strong nonlinearity. The hydrodynamic ram effect caused by debris hypervelocity impact on satellite tanks is unclear, and the influence of debris angular velocity on the hydrodynamic ram effect has also been rarely studied. In the present work, based on the ALE algorithm in the ANSYS/LS-DYNA software, a numerical simulation was carried out in which the spherical debris impacted the satellite tank at the velocity of 7000 m/s. The attenuation law of debris velocity, the propagation process of the shock wave, and the deformation of walls were investigated. The influences of the liquid filling ratio, magnitude, and direction of the debris angular velocity on the hydrodynamic ram effect were analyzed. The proposed method attempts to give a general modeling procedure that can be taken into account for similar numerical simulations. Attention is drawn to the material models and failure criteria for describing material behavior, to the connections of the debris/tank and debris/liquid, and to the geometrical meshing [18]. Moreover, numerical modeling of the satellite tank under hypervelocity impact can provide a beneficial reference for the structural design, and the need to validate the numerical models based on hypervelocity test data is emphasized.

2. Validation of Simulation Model

Details of hypervelocity impact tests conducted by NASA are confidential, so only part of the test phenomenon can be found in public reports. There are no quantitative test data to validate the simulation model. At present, the material parameters, boundary conditions, and contact definitions in a high-speed impact simulation model have mainly been validated based on the Varas test [9]. In the test, the projectile is spherical with a diameter of 1.25 cm and an impact velocity of 900 m/s. The tank is rectangular with dimensions of 75 cm, 15 cm, 15 cm, and 0.25 cm in length, width, height and wall thickness, respectively. The test device is displayed in Figure 1.

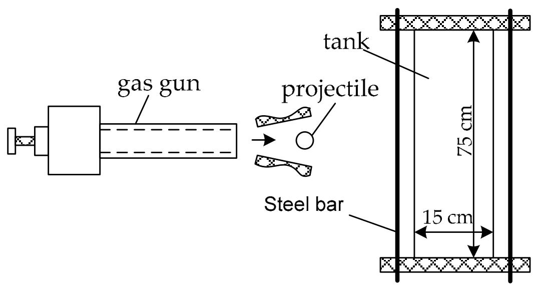

Figure 1. Schematic diagram of the Varas test device.

The simulation model consisted of the projectile, tank, water, and air. The tank walls were divided into the entry wall, exit wall, and lateral walls. Lagrange grids were constructed for the projectile and tank, whilst Euler grids were constructed for the water and air. These two grids were coupled through the ALE algorithm [14]. The interaction between the projectile and tank wall was achieved through the eroding surface-to-surface contact, and the interaction between the projectile and water was achieved through the automatic surface-to-surface contact. The non-reflecting boundary conditions were applied to the air boundary interfaces to prevent the shock wave from reentering the air field. Water was allowed to flow into the air region by sharing nodes on their interfaces. The mesh sizes of the projectile, tank walls, water, and air were 0.1 cm, 0.2 cm, 0.4 cm, and 2 cm, respectively. The whole model consisted of 377,605 elements. SOLID 164 elements with eight nodes were adopted, and each node had three DOFs. The computing time step was 0.6 μs. The simulation model and its local magnification diagram are exhibited in Figure 2.

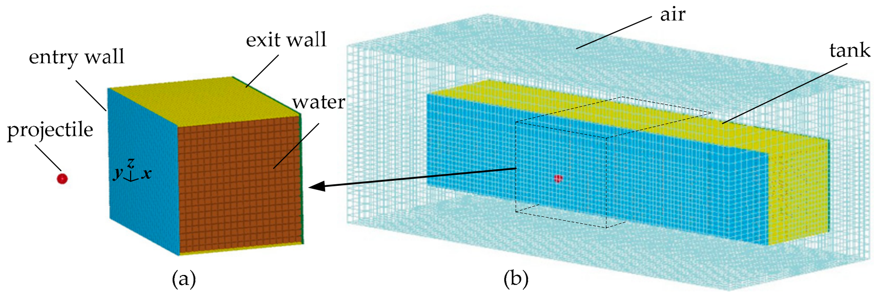

Figure 2. (**a**) Local magnification diagram of the simulation model. (**b**) The simulation model of the Varas test.

The air was modeled using the constitutive equation of MAT_NULL and the state equation of EOS_LINEAR_POLYNOMIAL [14]. The linear polynomial equation of state is linear in internal energy. The pressure P is given as follows:

$$P = C_0 + C_1\mu + C_2\mu^2 + C_3\mu^3 + (C_4 + C_5\mu + C_6\mu^2)E \tag{1}$$

where C_0~C_6 are the polynomial equation coefficients and $\mu = (\rho/\rho_0) - 1$, ρ/ρ_0 is the ratio of the current density to initial density. The air is considered as an ideal gas by setting $C_0 = C_1 = C_2 = C_3 = C_6 = 0$.

The water was modeled using the constitutive equation of MAT_NULL and the state equation of EOS_GRUNEISEN [14]. The Gruneisen equation with cubic shock velocity-particle velocity (v_s–v_p) defines pressure P as follows:

$$P = \frac{\rho_0 C^2 \mu\left[1 + \left(1 - \frac{\gamma_0}{2}\right)\mu - \frac{a}{2}\mu^2\right]}{\left[1 - (S_1 - 1)\mu - S_2\frac{\mu^2}{\mu+1} - S_3\frac{\mu^3}{(\mu+1)^2}\right]^2} + (\gamma_0 + a\mu)E \tag{2}$$

where S_1~S_3 are the slope coefficients of the v_s–v_p curve and γ_0 is the Gruneisen gamma. The properties and parameters for the water and air are listed in Table 1 [14].

Table 1. Material parameters of the water and air.

Material	ρ **(kg/m^3)**	S_1	S_2	S_3	γ_0	C_4	C_5
Water	1000	1.979	0	0	0.11	—	—
Air	1.29	—	—	—	—	0.4	0.4

The steel projectile and aluminum tank were modeled using the constitutive equation of MAT_JOHNSON_COOK and the state equation of EOS_GRUNEISEN. Johnson and Cook express the flow stress σ_y as follows:

$$\sigma_y = (A + B(\bar{\varepsilon}^p)^n(1 + C\ln\varepsilon^*)\left[1 - (T^*)^m\right] \tag{3}$$

where A is the quasi-static yield stress; B is the strain hardening modulus; and C, n, m are the material constants. These equations are widely used for metallic materials because numerous efforts have been exerted to determine the parameters. The material properties and parameters used for aluminum [14] and steel [19] are summarized in Table 2.

Table 2. Material parameters of the aluminum and steel.

Material	ρ **(kg/m^3)**	A **(MPa)**	B **(MPa)**	n	C	m
Aluminum	2700	200	144	0.62	0.01	1.00
Steel	7830	496	434	0.307	0.008	0.804

Figure 3 presents a comparison between the simulation results and test results at t = 84 µs and t = 140 µs. The three graphs in Figure 3 are the pressure nephogram of the shock wave in water (a), the sectional view on the *xoz* plane (b), and the picture captured by a high-speed camera in the Varas test (c) [9].

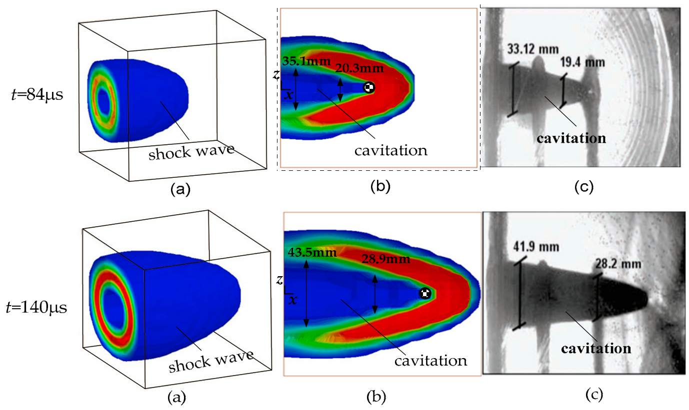

Figure 3. (**a**) Pressure nephogram of the shock wave in water. (**b**) Sectional view on the *xoz* plane. (**c**) Picture captured by a high-speed camera in Varas test [9].

In the simulation results, the cavity diameter at the distance of x from the impact point is expressed as d_s; the cavity diameter recorded by a high-speed camera is expressed as d_e; and the relative error between d_s and d_e is expressed as ε. The simulation results and test results are shown in Table 3. Table 3 indicates that d_s is larger than d_e at the same time. On one hand, the material parameters of the simulation model are inevitably different from the real situation in the test. On the other hand, part of the projectile kinetic energy is converted into the kinetic energy and the internal energy of water and the temperature of water rises. However, the temperature field was not considered in the numerical simulation, so the kinetic energy of projectile was completely converted into the kinetic energy of water. The radial velocity of water increased, which resulted in a larger cavity diameter at the same time. Overall, the relative error between the simulation results and test results was less than 10%, which validates the effectiveness of the simulation model.

Table 3. Cavity diameter in the simulation results and test results.

t (µs)	x (cm)	d_s (mm)	d_e (mm)	ε/%
84	1.5	35.1	33.12	5.9
	5.0	20.3	19.4	4.6
140	2.0	43.5	41.9	3.8
	7.5	28.9	28.2	2.5

3. Numerical Simulation of the Debris Impact on Satellite Tank

3.1. Simulation Model of the Debris Impacting Satellite Tank

Space debris comes from an invalid spacecraft, the final stages of a rocket, and disintegration debris, which are mainly made of aluminum. Satellite tanks are made of titanium and filled with liquid hydrazine with dimensions of 50 cm in diameter, 120 cm in height, and 2 mm in wall thickness. A numerical simulation was conducted with ANSYS/LS-DYNA software to reproduce a hypothetical scenario where spherical aluminum debris with a radius of 2 cm impacted the satellite tank at the velocity of 7000 m/s in the x direction. The impact point was located at the middle of the satellite tank. To study the most serious damage caused by the debris impact on satellite tank, the deformation of debris was neglected and the shape of debris was assumed to have remained unchanged.

The simulation model consisted of the debris, satellite tank, and liquid hydrazine, as displayed in Figure 4. Lagrange grids were constructed for the debris and tank, whilst Euler grids were constructed for the liquid hydrazine. The coupling between the Lagrange and Euler grids was realized by the key word CONSTRAINED_LAGRANGE_IN_SOLID. The interaction between the debris and tank wall was achieved through the eroding surface-to-surface contact, and the interaction between the debris and liquid hydrazine was achieved through the automatic surface-to-surface contact. The mesh sizes of the debris, satellite tank, and liquid hydrazine were 0.4 cm, 2 cm, and 2 cm, respectively. The whole model consisted of 96,848 elements. The computing time step was 0.6 μs.

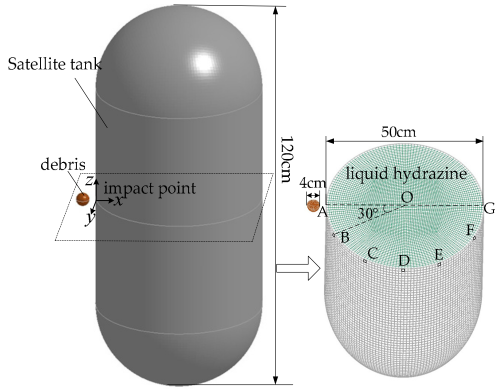

Figure 4. The simulation model of the debris impacting the satellite tank at the velocity of 7000 m/s; the right side is the model cut in half.

Since the density, boiling point, and critical temperature of liquid hydrazine are within 2% of the values for water [20], the constitutive equation MAT_NULL and the state equation EOS_GRUNEISEN of water were used to describe the liquid hydrazine. The material parameters of liquid hydrazine are listed in Table 4.

Table 4. Materials parameters of liquid hydrazine.

Material	ρ (kg/m^3)	C_l (m/s)	S_1	S_2	S_3	γ_0
Liquid hydrazine	1008	1500	1.979	—	—	0.11

As the parameters describing titanium in the Johnson Cook model are unknown, the titanium tank was modeled using the material model MAT_PLASTIC_KINEMATIC. The material model uses equivalent stress as the failure criterion. If the equivalent stress of Lagrange grids exceeds the yield strength of titanium, the failure elements will be deleted from the calculation program. This model was used to characterize the perforation on tank walls. The material parameters of titanium are listed in Table 5 [21] where E is the Young's modulus; υ is the Poisson's ratio; σ_s is the yield strength; and σ_b is the tensile strength.

Table 5. Material parameters of titanium.

Material	ρ (kg/m^3)	E (GPa)	υ	σ_s (MPa)	σ_b (MPa)
Titanium	4500	118	0.34	820	890

3.2. *Velocity Attenuation of Debris*

The velocities of debris at different times obtained by the simulation results are shown in Figure 5. When the debris moves in the liquid hydrazine, it is subjected to drag force, leading to a decrease in velocity [22]. The debris velocity attenuated sharply from 7000 m/s to 805 m/s at $0 < t < 200$ μs. The kinetic energy lost by the debris was mainly converted into the kinetic energy of the liquid hydrazine and the deformation energy of the tank walls. Liquid hydrazine begins to flow, and perforations and bulges occur on the front wall. The debris velocity decreased slowly at 200 µs < t < 800 µs, and the kinetic energy of debris was mainly used for the cavity expansion. At t > 800 µs, the debris velocity remained basically unchanged. When t = 1196 µs, the debris passed through the tank, the velocity decreased slightly, and a perforation occurred on the back wall. The residual velocity of the debris was 263 m/s, which indicates that the debris velocity is significantly reduced by the hydrodynamic ram effect.

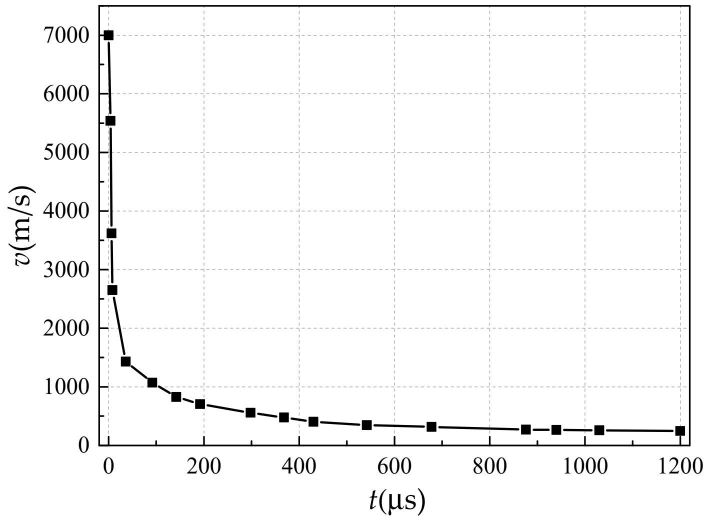

Figure 5. The velocities of debris at different times obtained by the simulation results.

3.3. Shock Wave Propagation

Figure 6 exhibits the pressure nephogram of the shock wave in the satellite tank at 53 µs, 125 µs, 160 µs, and 248 µs. When the debris penetrates the satellite tank, a hemispherical shock wave is formed in front of the debris and a cavity is formed behind the debris. The velocity of the shock wave is higher than that of the debris, so the debris lags behind the shock wave. In the propagation process, the shock wave exerts a pressure load on the tank walls. The irreversible energy loss occurs on the wave front, which results in the continuous decrease in shock wave pressure. At the same time, the debris squeezes the liquid hydrazine in front, and a local high pressure zone is generated. When t = 248 µs, the shock wave reached the back wall of the satellite tank. After the shock wave transmission, the high pressure hydrazine in front of the debris acts on the back wall, and further exerts a pressure load on it.

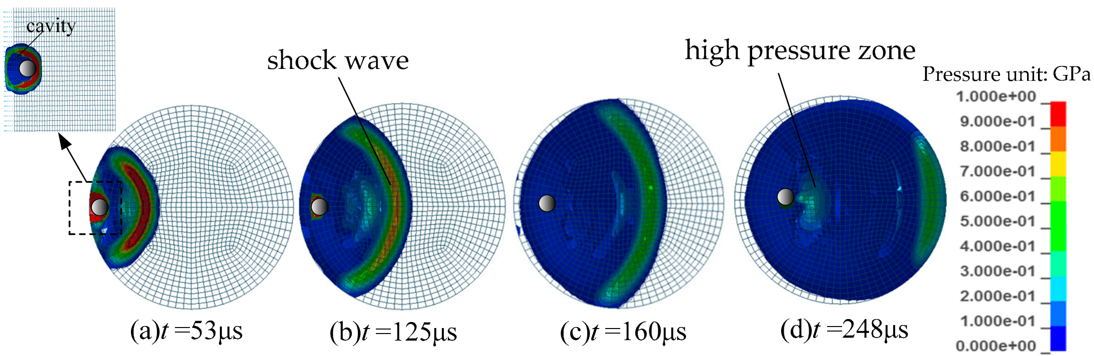

Figure 6. The pressure nephogram of the shock wave in the satellite tank at 53 µs, 125 µs, 160 µs, and 248 µs.

In order to study the pressure load exerted by the shock wave on the tank walls, element A~element G with the angles of 0°, 30°, 60°, 90°, 120°, 150°, and 180° to the impact line were selected respectively, as illustrated in Figure 4. The pressure–time curves from element A to element G are plotted in Figure 7.

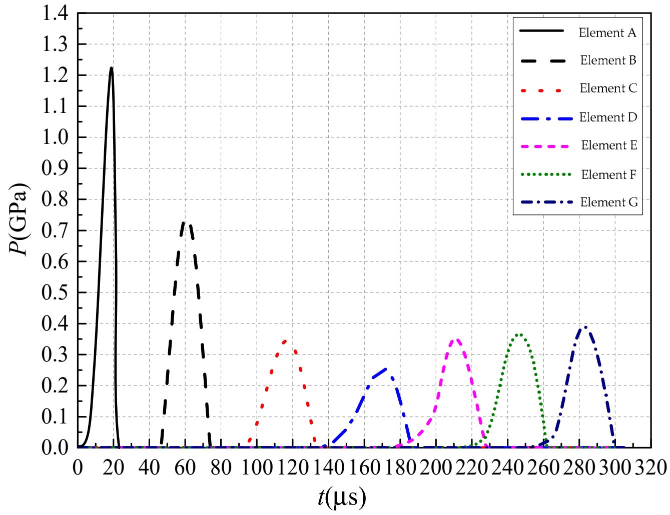

Figure 7. Pressure–time curves from element A to element G.

Element A was located at the impact point on the front wall. The pressure of the initial shock wave was the highest, which reached 1.22 GPa. In the propagation process, the shock wave compressed liquid hydrazine and exerted a pressure load on the tank walls. The energy of the wave front was irreversibly dissipated, the shock wave pressure decreased rapidly before element C, and decreased slowly after element C. Due to the superposition of the incident wave and reflected wave, the shock wave pressure increased from element D to element G. As the angle between element D and the impact line was 90°, the incident angle of shock wave was the smallest, the pressure of the reflected wave was the smallest, and the pressure of the superimposed wave front was also the smallest, which was only 260 MPa. Affected by the circumference, the incident angle from element D to element G increased gradually. Element G was located at the exit point on the back wall, and the shock wave reflection at element G was close to the positive reflection. After the superposition of the incident wave and reflected wave, the shock wave pressure reached 390 MPa.

3.4. Perforation of Front and Back Walls

When the debris impacted the front wall of the satellite tank, the stress concentration occurred at the impact point. The initial pressure of the shock wave was 1.22 GPa, which exceeded the yield strength of titanium (σ_s = 820 MPa). The failure elements were deleted, and circular perforation was generated on the front wall. The radial motion of the liquid hydrazine produced a pressure field that extruded the front wall. The deformation range of the front wall enlarged, resulting in an outward bulge.

The shock wave first arrived at the back wall and exerted pre-stress on it. However, the pressure of the shock wave decreased to 390 MPa, which was less than the yield strength of titanium. Plastic deformation occurred and an outward bulge was generated. After the transmission of the shock wave, the high pressure hydrazine in front of the debris acted on the back wall, and exerted a pressure load on it, which magnified the bulge height. The pressure applied by high pressure hydrazine on the back wall was also less than the yield strength, and no perforation was found. The penetration of debris was the main cause of perforation on the back wall.

The perforation and bulge on the front wall is displayed in Figure 8a, and the perforation and bulge on the back wall is displayed in Figure 8b. The maximum diameter of perforation is represented by d_{max}, and the bulge height is represented by δ. The perforation on the front wall was mainly caused by the high-pressure shock wave, the maximum diameter of which was d_{max} = 10.23 cm. The perforation on the back wall was mainly caused by debris penetration at the velocity of 263 m/s, the maximum diameter of which was d_{max} = 6.90 cm. Consequently, the diameter of perforation on the back wall was smaller than that on the front wall.

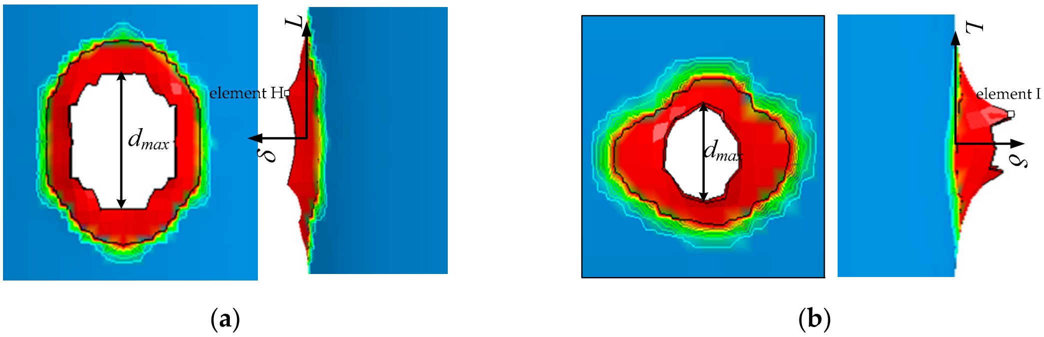

Figure 8. (**a**) Perforation and bulge on the front wall. (**b**) Perforation and bulge on the back wall.

Taking the distance from the impact point L as the abscissa and the bulge height δ as the ordinate, the curves of the bulge height varying with distance on the front and back walls were plotted in Figure 9. The curve was symmetrical with respect to the impact point (L = 0) and its shape was close to "M". The bulge range on the front wall was larger than that on the back wall, but the bulge height on the front wall was smaller than that on the back wall. The reason is that the bulge on the front wall was mainly caused by liquid hydrazine extrusion, while the bulge on the back wall was the result of the shock wave, high pressure hydrazine, and debris penetration. The bulge height at the edge of perforation was the largest. The maximum bulge height on the front wall was δ = 1.12 cm, and the maximum bulge height on the back wall was δ = 1.58 cm.

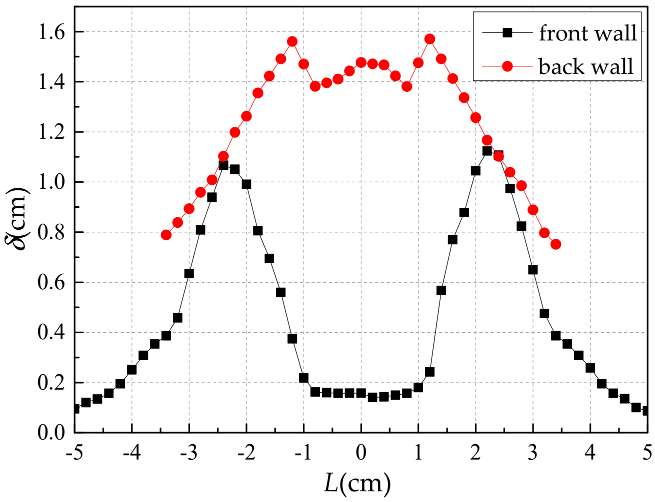

Figure 9. Curves of the bulge height varying with distance on the front and back walls.

4. Influence of Liquid-Filling Ratio on Hydrodynamic Ram Effect

4.1. Simulation Modes with Different Liquid-Filling Ratios

Liquid hydrazine will be consumed when the satellite maneuvers or changes orbit, so the satellite tank is not always full. Numerical simulations were conducted in which the spherical aluminum debris with a radius of 2 cm impacted satellite tanks filled with 70%, 80%, and 90% liquid hydrazine at the velocity of 7000 m/s and the damage of the satellite tanks caused by the hydrodynamic ram effect was studied.

Liquid hydrazine is squeezed out by high pressure nitrogen, and the satellite tank is filled with nitrogen and liquid hydrazine. Simulation models of the satellite tanks with liquid-filling ratios of 70%, 80%, and 90% are depicted in Figure 10. Lagrange grids were constructed for the debris and satellite tank, whilst Euler grids were constructed for the nitrogen and liquid hydrazine. A multi-material ALE formulation with a second-order accurate advection was selected to treat the nitrogen and liquid hydrazine. The liquid hydrazine was allowed to flow into the nitrogen region through shared nodes on their interfaces. The interaction between the debris and tank wall was achieved through the eroding surface-to-surface contact, and the interaction between the debris and liquid hydrazine was achieved through the automatic surface-to-surface contact. The mesh sizes of the debris, satellite tank, nitrogen, and liquid hydrazine were 0.4 cm, 2 cm, 2 cm, and 2 cm, respectively. The computing time step was 0.6 μs.

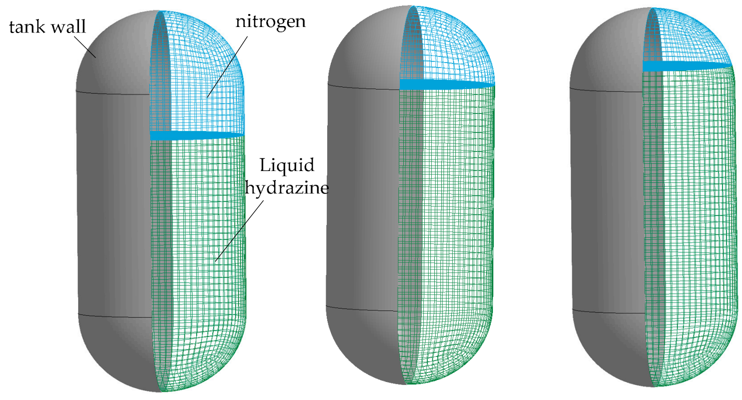

Figure 10. Simulation models of the satellite tanks with liquid-filling ratios of 70%, 80%, and 90%.

4.2. Perforation and Stress on Front and Back Walls

After the debris penetrated the satellite tanks with liquid-filling ratios of 70%, 80%, 90%, and 100%, the diameters of the front and back perforations, the bulge heights on the front and back walls were recorded and are summarized in Table 6. For a satellite tank with the same filling ratio, the diameter of the front perforation was larger than that of the back perforation, and the bulge height on the front wall was smaller than that on the back wall. For satellite tanks with different liquid-filling ratios, with the reduction in the liquid-filling ratios, the diameters of the front and back perforations decreased and the bulge heights on the front and back walls diminished, indicating that the damage caused by the hydrodynamic ram effect weakened.

Table 6. Perforation diameters and bulge heights at different liquid-filling ratios.

Deformation (cm)	100%	90%	80%	70%
Diameter of front perforation	10.23	9.46	9.20	9.08
Diameter of back perforation	6.90	6.24	5.51	5.05
Bulge height on front wall	1.12	0.99	0.79	0.71
Bulge height on back wall	1.58	1.45	1.33	1.29

The stress–time curves of element H (Figure 8a) on the front wall with liquid-filling ratios of 70%, 80%, 90%, and 100% are shown in Figure 11. The stress–time curves of element I (Figure 8b) on the back wall with liquid-filling ratios of 70%, 80%, 90%, and 100% are shown in Figure 12. When the debris impacted the front wall, the stress on the front wall rapidly reached the maximum under the action of the shock wave. Subsequently, stress oscillation occurred due to the extrusion of liquid hydrazine on the front wall. When the shock wave arrived at the back wall, the stress on the back wall reached the first peak, then high pressure hydrazine in front of the debris exerted a pressure load on the back wall, resulting in multiple stress peaks. At the moment of debris penetration, the stress on the back wall reached the maximum.

As can be seen from Figures 11 and 12, at the same time, the smaller the filling ratio, the smaller the stress on the front and back walls. This is because nitrogen acts as a buffer layer between the liquid hydrazine and the tank wall. As the liquid-filling ratio decreases, the gas volume increases, and the compressible space of the liquid hydrazine enlarges. The shock wave compresses the liquid hydrazine, then the liquid hydrazine compresses the nitrogen. The energy of the liquid hydrazine squeezing tank wall is dispersed, and the pressure load exerted on tank wall is reduced. In a word, the nitrogen in satellite tank diminishes the stress on the wall by reducing the pressure load exerted by liquid hydrazine, thus alleviating the damage caused by the hydrodynamic ram effect.

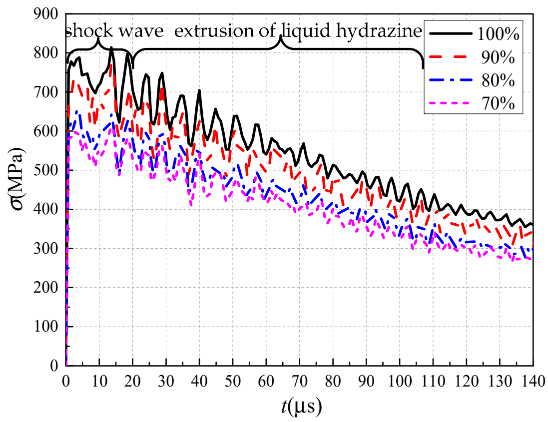

Figure 11. Stress–time curves of element H on the front wall with liquid-filling ratios of 70%, 80%, 90%, and 100%.

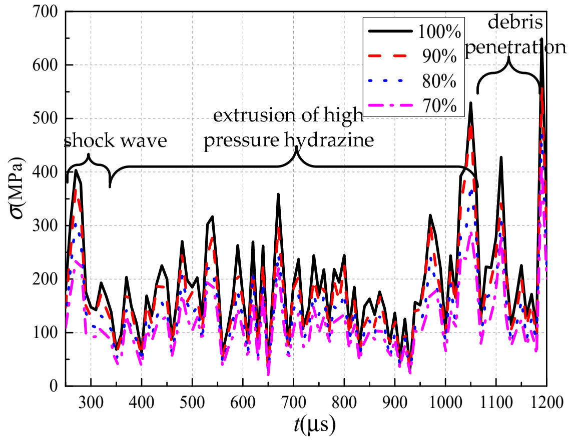

Figure 12. Stress–time curves of element I on the back wall with liquid-filling ratios of 70%, 80%, 90%, and 100%.

5. Influence of Angular Velocity on Hydrodynamic Ram Effect

Space debris produced by the explosion or disintegration of spacecraft not only has translational velocity, but also angular velocity. When space debris with an angular velocity impacts the satellite tank, the direction and magnitude of angular velocity can affect the hydrodynamic ram effect.

5.1. Influence of Angular Velocity Direction on Hydrodynamic Ram Effect

Numerical simulations were carried out in which the translation velocity of 7000 m/s in the x direction remained unchanged. The angular velocities of w_x = 5 rad/μs, w_y = 5 rad/μs, and w_z = 5 rad/μs were applied to the debris, respectively, and the influence of angular velocity direction on the hydrodynamic ram effect was studied.

Front and back perforations caused by the debris impacting satellite tank with angular velocities were compared with those caused by the debris impacting the satellite tank without angular velocities, which are illustrated in Figure 13. When the debris impacted the satellite tank at the angular velocity of w_x = 5 rad/μs, the front perforation was close to a quadrilateral, and the periphery was serrated. The absence of the back perforation indicates that the velocity declined to zero before the debris reached the back wall. When the debris impacted the satellite tank at the angular velocity of w_y = 5 rad/μs, the front perforation was elliptical, and the back perforation deviated from the initial impact point in the negative direction of the z axis. When the debris impacted the satellite tank at the angular velocity of w_z = 5 rad/μs, the front perforation was elliptical, and the back perforation deviated from the initial impact point in the negative direction of the y axis. Moreover, the front and back perforations caused by the impact of debris with angular velocities of w_x = 5 rad/μs, w_y = 5 rad/μs and w_z = 5 rad/μs were larger than those caused by the impact of debris without angular velocities, which indicates that the damage caused by the impact of debris with angular velocities is more serious.

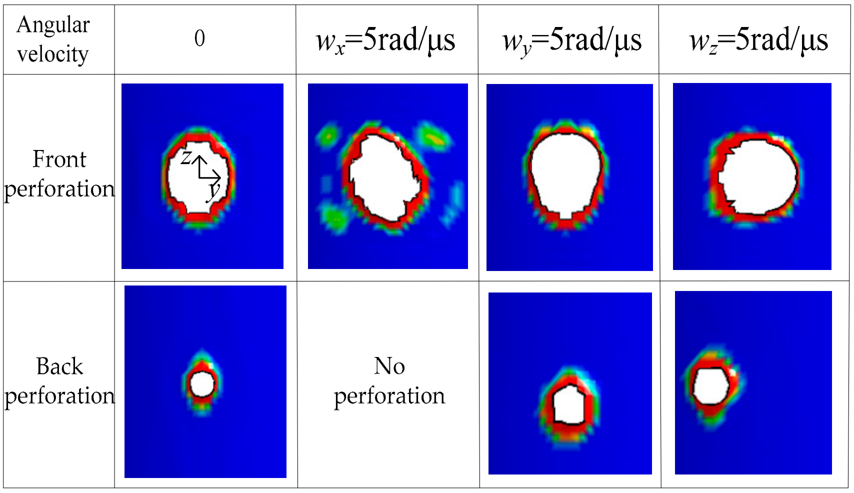

Figure 13. Front and back perforations caused by the debris impacting the satellite tank with angular velocities of w_x = 5 rad/μs, w_y = 5 rad/μs, and w_z = 5 rad/μs.

When the debris impacted the satellite tank with the angular velocities in the y and z direction, the back perforation deviated from the initial impact point, demonstrating that the direction of angular velocity has a significant effect on the debris trajectory.

When the debris penetrated the satellite tank with the angular velocity of w_x = 5 rad/μs, the debris trajectory is shown in Figure 14. The debris moved in the liquid hydrazine, and the liquid hydrazine flowed around the debris. The debris rotated around the x axis, and the surrounding liquid hydrazine produced a clockwise vortex around the x axis. The rotational direction of the vortex was perpendicular to the flow direction of the liquid hydrazine, no Magnus force was formed. The debris was only subject to liquid resistance, and the direction of translational velocity was not deflected. Under the action of viscous shear force, the velocity of the fluid layer around the debris decreased. Finally, the fluid layer adhered to the debris to form a boundary layer. The boundary layer enlarged the effective cross-sectional area of debris, leading to an increase in the liquid resistance, and a decrease in the debris velocity. As a result, the translation velocity decreased to zero at x = 35 m, and the debris could not pass through the back wall.

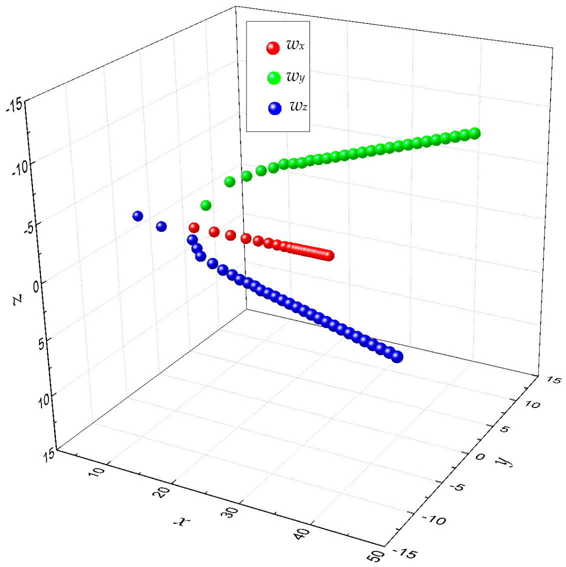

Figure 14. Debris trajectory when the debris penetrated the satellite tank with the angular velocities of w_x = 5 rad/μs, w_y = 5 rad/μs, and w_z = 5 rad/μs.

When the debris moves in liquid hydrazine, a boundary layer is formed around the debris and the turbulent wake is generated at the tail of the debris [23]. As the liquid flows back along the boundary layer, the kinetic energy in the boundary layer is dissipated by the viscosity. The velocity of the liquid decreases, which leads to an adverse pressure gradient in the boundary layer. Under the action of the adverse pressure gradient, the liquid slows down further. Finally, the kinetic energy of the liquid in the boundary layer is insufficient to maintain the downstream flow. Thus, boundary layer separation occurs. The shape of the boundary layer is symmetrical and the maximum thickness lies behind the debris, as shown in Figure 15a.

When the debris rotates around the y axis, the surrounding liquid hydrazine generates a clockwise vortex around the y axis [24]. The velocity direction of the vortex below the debris is the same as that of liquid, and the velocity of the liquid increases. The separation of the boundary layer accelerates, the separation point moves backwards, and the shape of the boundary layer is no longer symmetrical. The velocity direction of the vortex above the debris is opposite to that of liquid, and the velocity of the liquid decreases. According to the Bernoulli equation, the decrease in liquid velocity leads to the increase in pressure, and the increase in liquid velocity leads to the decrease in pressure. The pressure difference above and below the debris generates the Magnus force, which is shown in Figure 15b. Under the action of the Magnus force, the trajectory of debris deflects to the negative direction of the z axis, which is consistent with Figure 14.

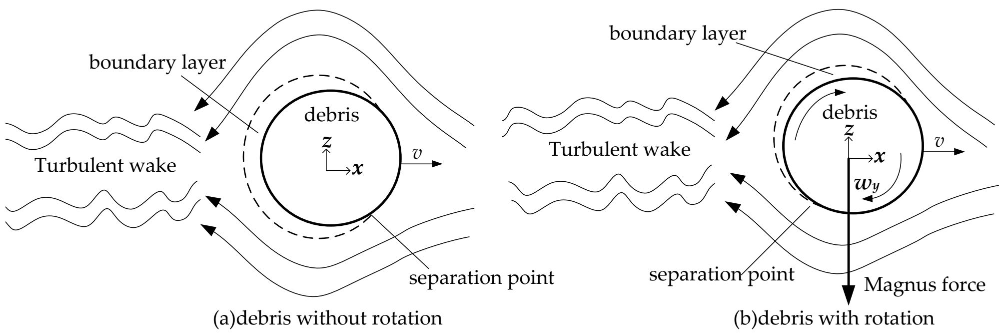

Figure 15. Flow patterns for liquid hydrazine past the debris without rotation (**a**) and the debris with rotation (**b**).

The debris trajectory when the debris penetrated the satellite tank with the angular velocity of w_z = 5 rad/μs is shown in Figure 14. When the debris rotated around the z axis, the surrounding liquid hydrazine generated a clockwise vortex around the z axis. The velocity direction of the vortex on the left side of the debris was opposite to that of the liquid flow, the velocity of liquid decreased, and the pressure of the liquid increased. However, the velocity direction of the vortex on the right side of debris was the same as that of the liquid flow, the velocity of liquid increased, and the pressure of the liquid decreased. The pressure difference on the left and right sides produced a transverse Magnus force. Under the action of the Magnus force, the trajectory of debris deflected to the negative direction of the y axis.

5.2. Influence of Angular Velocity Magnitude on the Hydrodynamic Ram Effect

The magnitude of angular velocity in the x direction directly affects the attenuation of the translation velocity, and determines whether the debris can pass through the satellite tank. Numerical simulations were conducted by setting the angular velocity in the x direction as w_x = 0.01 rad/μs, w_x = 0.05 rad/μs, w_x = 0.1 rad/μs, w_x = 0.5 rad/μs, w_x = 1 rad/μs, w_x = 2 rad/μs, w_x = 3 rad/μs, and w_x = 4 rad/μs. Figure 16 shows the front and back perforations caused by the impact of debris with different angular velocities in the x direction.

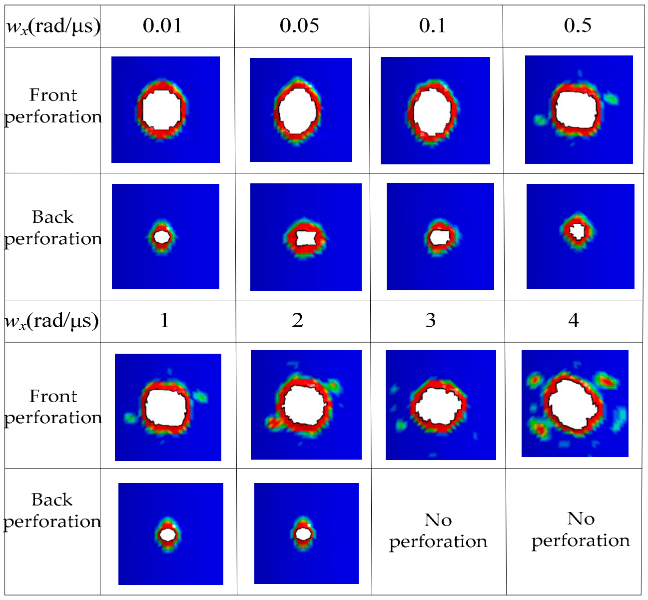

Figure 16. Front and back perforations caused by the impact of debris with angular velocities of w_x = 0.01 rad/μs, 0.05 rad/μs, 0.1 rad/μs, 0.5 rad/μs, 1 rad/μs, 2 rad/μs, 3 rad/μs, and 4 rad/μs.

When the debris impacted the satellite tank with the angular velocity of w_x < 2 rad/μs, it could pass through the back wall and the perforation was formed. However, when the debris impacted the satellite tank with the angular velocity of w_x > 3 rad/μs, it could not pass through the back wall. The reason is that with the increase of the angular velocity, the thickness of boundary layer increases, so the cross-section area of the debris enlarges. The kinetic energy of debris brought by the angular velocity cannot overcome the liquid resistance, and the debris velocity decays to zero in the tank.

Figure 17 depicts the attenuation curves of the translation velocity when the debris impacted the satellite tank with angular velocities of w_x = 0.01 rad/μs, 0.05 rad/μs, 0.1 rad/μs, 0.5 rad/μs, and 1 rad/μs. When w_x increased from 0.01 rad/μs to 0.05 rad/μs, the residual velocity of debris increased from 237 m/s to 334 m/s, but when w_x increased from 0.05 rad/μs to 1 rad/μs, the residual velocity of debris decreased gradually. When w_x = 0.05 rad/μs, the back perforation was the largest, which is consistent with Figure 16. The physical parameters of the liquid hydrazine were close to that of water. The reason for this phenomenon can be analyzed according to the conclusions of the rotating projectile entering water. Gu J. N. et al. [25] pointed out the projectile motion remained stable when the angular velocity reached w_l. The formula of w_l is as follows:

$$w_l = w_a \sqrt{\rho_l / \rho_a} \tag{6}$$

where ρ_l is the density of water; ρ_a is the density of air; and w_a is the angular velocity of the projectile moving steadily in the air.

When $0 < w_x < 0.05$ rad/μs, with the increase in angular velocity, the stability of the debris motion enhanced, and the attenuation effect of liquid resistance on debris velocity was weakened. When $w_x = w_l = 0.05$ rad/μs, the debris moved stably in liquid hydrazine and its residual velocity was the largest. As the angular velocity of debris increased, the rotational velocity of the vortex also enlarged. When the rotational kinetic energy brought by the angular velocity of the debris was not enough to maintain the vortex rotation, the kinetic energy brought by the translational velocity of debris will be further consumed, resulting in the attenuation of the translational velocity.

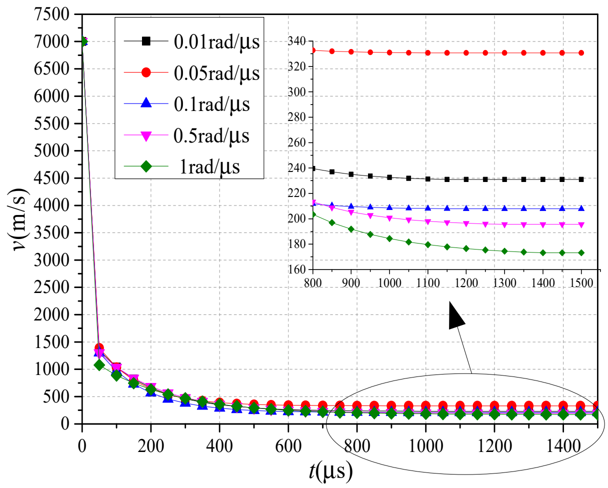

Figure 17. Attenuation curves of the translation velocity when the debris impacted the satellite tank with angular velocities of w_x = 0.01 rad/μs, w_x = 0.05 rad/μs, w_x = 0.1 rad/μs, w_x = 0.5 rad/μs, and w_x = 1 rad/μs.

When the debris impacts the satellite tank with the angular velocity in the *y* and *z* direction, the motion laws of debris are similar. In this section, the angular velocity in the *y* direction was taken as an example. Numerical simulations were conducted by setting the angular velocity in the *y* direction as w_y = 1 rad/μs, w_y = 2 rad/μs, w_y = 3 rad/μs, w_y = 4 rad/μs, and w_y = 5 rad/μs. Figure 18 shows the front and back perforations caused by the impact of the debris with different angular velocities in the *y* direction. Figure 19 depicts the attenuation curves of the translation velocity when the debris impacted the satellite tank with angular velocities of w_y = 1 rad/μs, 2 rad/μs, 3 rad/μs, 4 rad/μs, and 5 rad/μs.

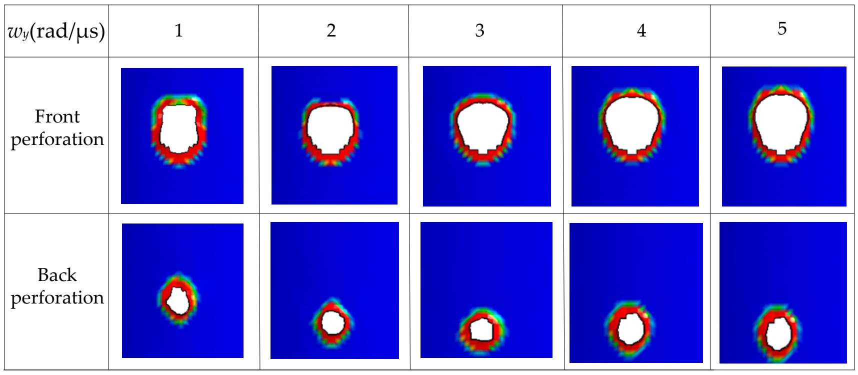

Figure 18. Front and back perforations caused by the impact of debris with angular velocities of w_y = 1 rad/μs, w_y = 2 rad/μs, w_y = 3 rad/μs, w_y = 4 rad/μs, and w_y = 5 rad/μs.

With the increase in angular velocity, the maximum diameter of the front perforation increased, and the shape of front perforation gradually evolved into the shape of water droplets. As seen in Figure 19, with the increase in angular velocity, the residual velocity of the debris increased, as did the diameter of the back perforation caused by debris perforation. This is because when the debris rotates around the *y* axis, the velocity direction of the vortex below the debris is the same as that of liquid. With the increase in angular velocity, the vortex velocity increases, the separation of boundary layer accelerates, and the separation point moves backwards. The area of boundary layer decreases, and the effective cross-sectional area composed of the debris area and boundary layer area also reduces, leading to a decrease in drag force and an increase in the residual velocity of the debris. Moreover, with the increase in angular velocity, the deviation of the back perforation in the negative direction of *z* axis increases. The reason is that the pressure difference above and below the debris increases, resulting in a larger Magnus force.

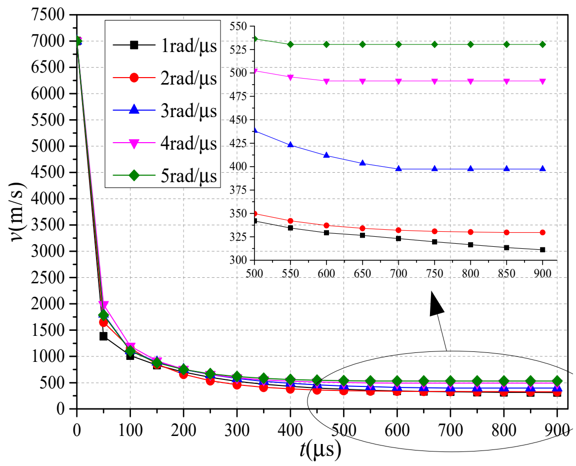

Figure 19. Attenuation curves of the translation velocity when the debris impacted the satellite tank with angular velocities of w_y = 1 rad/μs, w_y = 2 rad/μs, w_y = 3 rad/μs, w_y = 4 rad/μs, and w_y = 5 rad/μs.

6. Conclusions

- When the debris impacted the satellite tank at the velocity of 7000 m/s, it passed through the tank at t = 1196 μs, and the residual velocity was 263 m/s, indicating that the debris velocity was significantly reduced by the hydrodynamic ram effect.
- The shock wave pressure on the front wall was the highest, which exceeded the yield strength of titanium, so perforations and bulges occurred. Except for the front wall, the pressure on the tank walls was smaller than the yield strength of titanium. Under the action of debris penetration and

high pressure hydrazine, perforations and bulges also occurred on the back wall. In the structural design of the satellite tanks, the material strength of the walls should be increased as much as possible, and the protection should be strengthened in vulnerable areas.

- With the reduction in the liquid-filling ratios, the damage caused by the hydrodynamic ram effect weakened and the satellite tank fully-filled with liquid hydrazine was the most severely damaged.
- When the debris impacted the satellite tank with the angular velocities in the x direction, the debris trajectory did not deflect. When the debris impacted the satellite tank with the angular velocities in the y and z direction, the debris trajectory deflected to the negative direction of the z axis and y axis under the action of the Magnus force.
- There was a steady angular velocity in the x direction. Under the steady angular velocity, the damage to the tank was the most serious. With the increase in the angular velocity in the y and z direction, the damage to the tank became more serious.

Author Contributions: Conceptualization, C.C.; Methodology, J.Z.; Software, B.Z.; Validation, B.Z.; Formal analysis, B.Z.; Investigation, B.Z.; Resources, J.Z.; Data curation, C.C.; Writing—original draft preparation, B.Z.; Writing—review and editing, J.Z.; Visualization, Y.D.

Funding: This research received no external funding.

Acknowledgments: This research was done with the financial support of the State Key Laboratory of Laser Propulsion and Application. We wish to express our sincere gratitude to Dr. Wang for his valuable help.

Conflicts of Interest: The authors declare no conflicts of interest.

References

1. Shen, H.R.; Wang, W.J.; Li, Y.Y.; Shao, Q.L. *Modeling and Analysis of Spacecraft Impact*; Science Press: Beijing, China, 2014; p. 138.
2. Varas, D.; Lopez-piente, J.; Zaera, R. Numerical analysis of the hydrodynamic ram phenomenon in aircraft fuel tanks. *AIAA J.* **2012**, *50*, 1621–1630. [CrossRef]
3. Han, L.; Han, Q.; Yang, S. Simulation analysis of hydrodynamic ram in an aircraft fuel tank subjected to high-velocity muti-fragment impact. *Explos. Shock Waves* **2018**, *38*, 473–484.
4. Xu, S.X.; Wu, W.G.; Li, X.B.; Kong, X.S.; Huang, Y.L. Protective effect of guarding fluid cabin bulkhead under attacking by explosion fragment. *Explos. Shock Waves* **2010**, *30*, 395–400.
5. Varas, D.; Zaera, R.; Lopz-Puente, J. Numerical modelling of the hydrodynamic ram phenomenon. *Int. J. Impact Eng.* **2009**, *36*, 363–374. [CrossRef]
6. Disimile, P.J.; Swanson, L.A.; Toy, N. The hydrodynamic ram pressure generated by spherical projectiles. *Int. J. Impact Eng.* **2009**, *36*, 821–829. [CrossRef]
7. Townsend, D.; Park, N.; Devall, P.M. Failure of fluid filled structures due to high velocity fragment impact. *Int. J. Impact Eng.* **2003**, *29*, 723–733. [CrossRef]
8. Nishida, M.; Tanaka, K. Experimental study of perforation and cracking of water-filled aluminum tubes impacted by steel spheres. *Int. J. Impact Eng.* **2006**, *32*, 2000–2016. [CrossRef]
9. Varas, D.; Lopez-piente, J.; Zaera, R. Experimental analysis of fluid-filled aluminium tubes subjected to high-velocity impact. *Int. J. Impact Eng.* **2009**, *36*, 81–91. [CrossRef]
10. Ma, L.Y.; Li, X.D.; Zhou, L.W.; Zhang, G.F. Study on the characteristics of cavity formed by fragment impacting liquid filling container. *Explos. Shock Waves* **2018**, *38*, 235–241.
11. Kong, X.S.; Wu, W.G.; Li, J.; Li, X.B.; Xu, S.X. Effects of explosion fragments penetrating defensive liquid-filled cabins. *Explos. Shock Waves* **2013**, *33*, 471–478.
12. Aziz, M.R.; Kuntjoro, W.; David, N.V. Pressure history in hydrodynamic Ram (HARM) by using FEM-SPH approach. In Proceedings of the 6th International Conference on Control System, Computing and Engineering IEEE, Penang, Malaysia, 25–27 November 2016; pp. 108–112.
13. Kangjie, R.Y. *Simulation of Hydrodynamic Ram Phenomenon Using MSC Dytran*; Nanyang Technological University: Singapore, 2008.
14. Varas, D.; Zaera, R.; Lopz-Puente, J. Numerical modelling of partially filled aircraft fuel tanks submitted to hydrodynamic ram. *Aerosp. Sci. Technol.* **2012**, *16*, 19–28. [CrossRef]

15. Han, L.; Han, Q.; Yang, S. Simulation analysis of hydrodynamic ram factors and effects in aircraft fuel tank. *Adv. Aeronaut. Sci. Eng.* **2018**, *9*, 490–500.
16. Rucker, M.A.; Beeson, H.; Stoltzfus, J.M.; Frank, J.B. *Demonstration of Hazardous Hypervelocity Test Capability*; Report TR-692-001; White Sands Test Facility: Las Cruces, NM, USA, 1991.
17. Wilson, C.W.; Warne, D.; Chatfield, M.D. *Fuel Tank Explosion Lethality*; Report 91-5425-SH; Science Applications International Corporation: Reston, VA, USA, 1991.
18. Martin, L.; Michel, A.; Chiara, B.; Doormaal, J.C.A.M.; Christof, H.; Gotz, H.; Oliver, M.; Arja, S.; George, S.; Laurent, T.; et al. Design of Blast-Loaded Glazing Windows and Facades: A Review of Essential Requirements towards Standardization. *Adv. Civ. Eng.* **2016**, *2016*, 2604232.
19. Zhang, K.F.; Liang, M.Z.; Lu, F.Y.; Li, X.Y. Mechanics of plate fracture from detonation wave interaction. *Propell. Explos. Pyrot.* **2019**, *44*, 188. [CrossRef]
20. Garcia, B.O.; Chavez, D.J. Shock compression of liquid hydrazine. In Proceedings of the 1995 Shock Compression Conference, Seattle, WA, USA, 15–18 August 1995.
21. Li, Y.F.; Jin, Q.C.; Liu, Z.D.; Li, G. Finite element analysis of a propellant satellite tank based on ANSYS. *Aerosp. Manuf. Technol.* **2012**, *12*, 10–15.
22. Lecysyn, N.; Bony, D.A.; Aprin, L.; Heymes, F.; Slangen, P.; Dusserre, G.; Munier, L.; Gallic, C.L. Experimental study of hydraulic ram effects on a liquid storage tank: Analysis of overpressure and cavitation induced by a high-speed projectile. *J. Hazard. Mater.* **2010**, *178*, 635–643. [CrossRef] [PubMed]
23. Munson, B.R.; Young, D.F.; Okiishi, T.H.; Huebsch, W.W. *Fundamentals of Fluid Mechanics*, 6th ed.; Wiley: Hoboken, NJ, USA, 2009; pp. 500–503.
24. Lei, J.M.; Li, T.T.; Huang, C. A numerical investigation of Magnus effect for high-speed spinning projectile. *Acta Armam* **2013**, *34*, 718–725.
25. Gu, J.N.; Zhang, Z.H.; Fan, W.J. Experimental study on the penetration law for a rotating pellet entering water. *Explos. Shock Waves* **2005**, *25*, 341–349.